



Mechanistic insight into the quantitative synthesis of acetic acid by direct conversion of CH₄ and CO₂: An experimental and theoretical approach

Raghavendra Shavi^{a,1}, Jeonghyun Ko^{b,1}, Ara Cho^c, Jeong Woo Han^{c,*}, Jeong Gil Seo^{a,*}

^a Department of Energy Science and Technology, Myongji University, Nam-dong, Cheoin-gu, Yongin-si, Gyeonggi-do 17058, South Korea

^b Department of Chemical Engineering, University of Seoul, 163 Seoulsiripdaero, Dongdaemun-gu, Seoul 02504, South Korea

^c Department of Chemical Engineering, Pohang University of Science and Technology (POSTECH), 77 Cheongam-ro, Nam-gu, Pohang, Gyeongbuk 37673, South Korea

ARTICLE INFO

Keywords:

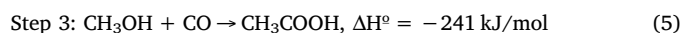
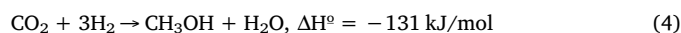
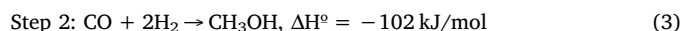
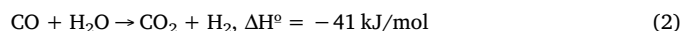
Methane activation
CO₂ Conversion
Carbonylation
Acetic acid
Mechanism

ABSTRACT

Conversion of CH₄ and CO₂ into value-added products has vital environmental and economic importance. Their direct conversion to acetic acid is challenging due to their high activation energy. Hence, kinetic and mechanistic information are crucial for the carbonylation of CH₄ with CO₂. Regarding this, single and dual component catalysts with different combinations of ZnO-, CeO₂-, and MnO₂- supported montmorillonite (MMT) were prepared and characterized by XPS, Raman, and XRD. Quick solid-state NMR, TGA, and FT-IR techniques were used and Langmuir-Hinshelwood model was considered to investigate mechanistic steps involved in the conversion of CH₄ and CO₂ to acetic acid. The obtained mechanistic and kinetic results were also theoretically proved by density functional theory (DFT) calculations. We found that ZnO and CeO₂ dual active sites preferentially adsorb the CH₄ and CO₂, respectively that avoid surface adsorption competition. The rate of acetic acid formation was maximum when these sites exist at appropriate concentration (Ce: 0.44 wt%, Zn: 2.20 wt%). DFT calculations elucidated that the formation of acetic acid is strongly favored on ZnO catalyst with easier migration of the adsorbed CO₂ from CeO₂ to the ZnO side.

1. Introduction

Research on converting abundant, unwanted, and global warming gases to value-added products has been attracting great attention as a critical challenge for mitigating climate change on earth. It is in the interest of science to develop solutions that maintain and promote a "green" earth. Many preliminary precautions, such as reducing coal burning, planting trees, have been taken to minimize pollution and global warming. However, in populous developing countries, such as China and India, coal utilization is still necessary to meet large energy demand. Therefore, steps must be taken to utilize byproducts from all types of polluting activities. To that end, the consumption of CH₄ and CO₂ seems a potential solution associated with climate change [1–8]. Activation and utilization of CH₄ have been widely studied [9–12]. However, research on its conversion to oxygenates, such as methanol, acetic acid, and formaldehyde, is limited due to the high bond energies of CH₄ ($\Delta H_{C-H} = 439.57 \text{ kJ mol}^{-1}$) and the lack of knowledge concerning catalyst properties and kinetic parameters involved in product formation mechanisms. Among oxygenates of CH₄, the preparation of acetic acid is much difficult as it requires three different reaction steps as shown below:



Each step reaction needs different types of catalysts and high temperature. Hence, the current focus is on forming acetic acid in a single step by direct conversion of CH₄ using a carbonylating agent such as CO or CO₂.

A perceptible work on the synthesis of acetic acid by carbonylating CH₄ in a single step has been achieved by utilizing noble metals [13–15] such as Pd [16] and Rh [17] catalysts. Few combined experimental and theoretical studies [18–21] have been performed in order to understand mechanism and kinetics of this reaction, as listed in Table 1. In the last decade, those noble metals have been replaced by 3d transition metals such as Cu [22] and Zn [23]. Both the active metals (Cu and Zn) are Lewis acids and CH₄ is capable to fragment over acidic

* Corresponding authors.

E-mail addresses: jwhan@postech.ac.kr (J.W. Han), jgseo@mju.ac.kr (J.G. Seo).

¹ These authors contributed equally to this work.

Table 1
Literature survey on various catalysis for acetic acid production.

Year	Catalyst	Carbonylating agent	Reaction system	Yield/Remark	Reference
2003	RhCl ₃	CO	Homogeneous	Expensive catalyst, Lower selectivity, needs promotor, complicated system	[18]
2006	Pd ²⁺	CO	Homogeneous	Expensive catalyst, Harsh reaction medium, complicated mechanism, No cyclic reaction	[19]
2007	Amavadinine related vanadium complexes	CO	Homogeneous	Harsh reaction medium, complicated mechanism,	[21]
2012	Au(I)-ZSM-5	CO ₂	Heterogeneous	Expensive catalyst, reactant adsorption competition,	[25]
2014	Rh	Syngas	Heterogeneous	Poor selectivity, Expensive catalyst, complicated mechanism	[20]
2017	ZnO-CeO ₂ /MMT	CO ₂	Heterogeneous	Easy system, cheap catalyst, cyclic mechanism, no reactant adsorption competition	This work

catalysts [15]. They also demonstrate an affinity for CO₂, forming surface carbonates. However, CO₂ is an acid itself. Hence, the concept of CO₂ adsorption on another acidic active metal site is unexpected and not easy to explain. Moreover in these cases, there exists a surface adsorption competition between two reactant gases CH₄ & CO₂. Such phenomena may slower the kinetic parameters of acetic acid formation reaction. The stability of intermediate anions over active site, their ionic attraction strength to the active site also contribute to the total transformation of the gases into products. Therefore, the size of active site, which accounts for strength of surface intermediate, would be a crucial parameter for this reaction. All these vital parameters have not been explored and thus there is no information about how to synthesize acetic acid in a quantitatively way.

There are few theoretical studies on the direct conversion of CH₄ and CO₂ to acetic acid [18,19,24,25]. Some researchers [24,25] used metal-exchanged zeolite catalysts, and identified that the active site of surface reaction is the exchanged metal atom. In addition, they analyzed that either CH₄ activation step [24] or CO₂ insertion step into the metal-CH₃ bond [25] is a possible rate-determining step (RDS). Meanwhile, Zhao et al. [26] investigated the direct conversion of CH₄ and CO₂ by using the Zn-doped ceria catalyst. They elucidated the active site is a doped-Zn atom onto the ceria, which reduces the activation energy for CO₂ insertion step into Zn-CH₃ bond that is the RDS. This is attributed to the destabilization of the Zn-CH₃ bond by low electronegativity of the doped Zn. However, these kinds of catalysts have only a single active site. On the contrary, a catalyst we are suggesting in this study has dual-active site, which is expected to have its unique catalytic behavior.

In this work, to avoid adsorption competition between gases, we prepared dual active-site catalysts containing two different metal oxides supported on montmorillonite (MMT) zeolite. Rabie et al., recently, reported the possibility of quantitative acetic acid formation over a catalyst with dual active sites [27]. As an extended step, we are pinpointing the above explained fundamental properties of catalyst that aid higher selectivity towards acetic acid. For the study, various catalysts (CeO₂-ZnO/MMT, MnO₂-ZnO/MMT, and CeO₂-MnO₂/MMT) were prepared by varying metal oxide combination to explore the effects of Lewis acidity, atomic size, reactant adsorption, and oxidizing properties. MMT was chosen for improving the dissociation of CH₄ on its oxygen sites as it is reported that CH₄ activation increases over oxygen rich surfaces [28]. Several experiments were performed to explore the importance of those fundamentals and a mechanism was deduced based on experimental outcome. The mechanism and energies of each intermediate steps were further calculated and ensured by density functional theory (DFT) calculations. Energies required for each step in forming acetic acid were calculated for both CeO₂ and ZnO, respectively. Results were well matched and confirmed that the experimentally drawn intermediates which are favorably formed over different active sites possess the lowest energy in DFT calculations as well. Hence, a generalization of factors that favor formation of higher acetic acid is drawn out as conclusions. Despite there are few DFT reports on this reaction over zinc and cerium catalysts [29], to the best of our knowledge, this is

the first attempt to study the reaction mechanism for acetic acid synthesis over catalyst having dual active sites.

2. Experimental

2.1. Starting materials

Cerium(III) nitrate hexahydrate (99%, Sigma-Aldrich), Zinc nitrate hexahydrate (98% Sigma-Aldrich), Manganese(II) nitrate tetrahydrate (> 97% Sigma-Aldrich), Montmorillonite K 10 powder (Sigma-Aldrich), Double distilled water, methane gas (99.95% purity), and carbon dioxide gas (99.999% purity) were used as received.

2.2. Catalyst preparation

1 g of montmorillonite zeolite was dispersed into 50 mL of water contained in a beaker. This system was stirred for 48 h with a magnetic bead at rate 600 rpm and was sonicated for 4 h to achieve well dispersion of zeolite nanolayers. To this solution, nitrate solutions of desired active metal with appropriate concentration were added. The particles solution was stirred further for 25 h. In the next step, the mixture was centrifuged, filtered and then washed with distilled water to remove additional ions from the metal surface. The product was dried at 110 °C and ground to fine powder. Finally, calcination was done at a ramping heat rate of 2.5 °C for 4 h 40 min to reach 700 °C in the air medium. The final temperature was further maintained for 1 h. Washings with water was avoided when particular concentration of metal oxide was required on support. Same procedure followed for single oxide supported catalysts keeping total moles of active site equal to that of dual component catalysts.

2.3. DFT calculations

We performed plane wave density functional theory (DFT) calculations by employing the Vienna Ab Initio Simulation Package (VASP) [30–33]. We used the Perdew-Burke-Ernzerhof (PBE) functional based on generalized gradient approximation (GGA) to treat the exchange-correlation energy [34]. To consider dispersion force, a semi-empirical DFT-D3 method proposed by Grimme was applied [35]. In the expansion of the plane wave, a kinetic cutoff energy of 400 eV was employed. The residual minimization method for electronic relaxation was exploited to calculate the total energy, which was accelerated using Methfessel-Paxton Fermi-level smearing [36] with a width of 0.05 eV, and spin polarization was considered in all calculations. Geometry optimization was carried out using a conjugate gradient algorithm until the forces on all unconstrained atoms were less than 0.03 eV/Å. To prevent an artificial electrostatic field, dipole corrections were applied in the surface normal direction to compute all energies reported here [37,38]. The GGA + *U* approach was employed to correctly describe the localized nature of the 4f electrons of Ce [39,40]. Here, a Hubbard parameter *U* value of 4.5 eV was selected based on previous studies [41,42]. Meanwhile, according to previous theoretical reports of the

physical properties of ZnO, [43,44] Hubbard U can also enhance the accuracy of the calculation by correcting the conventional GGA method's overestimation of the energy level of Zn 3d states. We thus applied a Hubbard parameter U value of 5.0 eV to Zn atoms [43,45].

Bulk CeO₂ has a fluorite structure with an experimental lattice value of $a = 5.411$ Å [46]. We obtained a DFT-optimized lattice parameter of $a = 5.476$ Å. On the other hand, bulk ZnO has a wurtzite structure, and the experimental lattice parameters of a and c are 3.258 and 5.220 Å respectively [47]. Our DFT-optimized lattice parameters of ZnO were $a = 3.214$ and $c = 5.175$ Å. For both metal oxides, the lattice parameters we obtained are in good agreement with the experimental values. In our surface models, CeO₂(111) was constructed by three O–Ce–O trilayers with a (2×2) surface unit cell while ZnO(10 $\bar{1}$ 0) was modeled with six atomic layers and a (2×1) surface unit cell. For both surfaces, the bottom three atomic layers were fixed in their bulk positions while the remaining atoms of each slab and their adsorbates were fully relaxed. A 15 Å of vacuum space was introduced to separate two neighboring slabs of each surface. The Monkhorst–Pack grids of $3 \times 3 \times 1$ and $2 \times 4 \times 1$ k -points were used for CeO₂(111) and ZnO(10 $\bar{1}$ 0), respectively. The adsorption energy, E_{ads} , is defined as

$$E_{\text{ads}} = E_{\text{total}} - E_{\text{surf}} - E_{\text{adsorbate}},$$

where E_{total} is the total energy of the system containing the adsorbed species, E_{surf} is the total energy for the optimized bare surface, and $E_{\text{adsorbate}}$ is the total energy for the adsorbate in the gas phase, respectively. Activation energies and the transition images for all elementary steps were calculated by using climbing image-nudge elastic band (CI-NEB) method [48]. The transition state (TS) configuration and minimum energy pathway were optimized using at least four intermediate images until the maximum atomic forces were converged less than 0.05 eV/Å. Each transition state was confirmed to have a single imaginary frequency along the reaction coordinate (Table S2 of the Supporting information). Furthermore, full coordinates of all optimized structures including adsorbates and transition states are listed in Tables S3–S33 of the Supporting information.

3. Results and discussion

3.1. Acetic acid quantification and experimental evidence

The acetic acid yield obtained over different catalysts at various temperatures are shown in Table 2. The MMT support alone employed

as catalyst was capable of activating methane under the provided reaction conditions. However, a very low concentration of formic acid, a byproduct, was detected while the formation of target product acetic acid was nil. High oxygen density on the zeolite MMT (63.83 at. % as noticed by XPS) may adsorb CO₂ that could form carbonates with the metal cations (K⁺, Fe²⁺, Mg²⁺, and etc.) which are being structurally trapped in nano-layered MMT (Fig. 1). Subsequently, these carbonates react with acidic surface hydroxyl groups to produce formic acid. Compared to dual active site catalysts, single active site catalysts showed poor activity for the production of acetic acid (Table 2). This might be due to different probabilities of surface adsorption and reaction pathways that depends on adsorption of reacting gases on the active sites (doped metal oxides). When CO₂ is adsorbed prior to CH₄ on active site, it could form formic acid as byproduct. In other words, a delay in the CH₄ adsorption may cause its dissociation that could supply hydrogen atoms to initially adsorbed CO₂, allowing the formation of formic acid. (Fig. S3b). Hence, it is meaningful to utilize a dual active site catalyst where CH₄ and CO₂ can be preferentially adsorbed over two chemically different active sites. Such adsorption could easily allow co-conversion of these two gases into acetic acid with high selectivity. Among dual active site catalysts, ZnO-doped catalysts showed better activity (Table 2) due to better selectivity of CH₄ towards ZnO as identified by solid state MAS ¹H NMR (Fig. 4) and confirmed by DFT calculations. System CeO₂-ZnO/MMT showed the best catalytic activity producing 0.35 mmol of acetic acid. The activity was followed by MnO₂-ZnO/MMT and CeO₂-MnO₂/MMT. To the best of our knowledge, CeO₂-ZnO/MMT catalyst performed the best catalytic activity in terms of acetic acid yield till the date.

The better activities of CeO₂-ZnO/MMT and MnO₂-ZnO/MMT catalyst could be understood by the presence of zinc oxide in common as a Lewis acid. In case of CeO₂-ZnO/MMT, carbonate formed on the bigger Ce atom (248 p.m.) might be highly reactive and readily transferable due to weaker dipole attraction between the carbonate anion and Ce atom, which favors a Langmuir-Hinshelwood type adsorption mechanism. In the MnO₂-ZnO catalyst, Mn may hold carbonate anion strongly due to its relatively smaller atomic size (205 p.m.), making it little difficult to transfer and hence showed moderate activity. The other possibility is that the active Zn metal was either dissolved in MnO₂ or unable to impart its activity in the reaction. As shown in XRD (Fig. S2), stronger CeO₂ peak in CeO₂-MnO₂/MMT catalyst found to be less pronounced. In MnO₂-doped catalysts, therefore, the involvement of co-active site in the reaction is slightly caught up causing lesser yield.

Table 2

The catalytic activity of different oxide supported systems. Reaction conditions: pressure, 2 bars, catalyst amount 0.2 g, reaction time, 2 h.

Catalyst	Total moles of active site	Temperature (K)	Acetic acid (CH ₃ COOH) (mmol)	TON ($\times 10^3$) ^a	CH ₄ conversion (%)
MMT	0.00	573	0.000	0	Negligible
CeO ₂ /MMT	2.5×10^{-4}	573	0.015	60	0.50
ZnO/MMT	2.5×10^{-4}	573	0.055	220	1.80
CeO ₂ + ZnO/MMT	2.5×10^{-4}	473	0.002	8	0.06
	2.5×10^{-4}	523	0.024	96	0.80
	2.5×10^{-4}	573	0.24	960	8.00
	2.5×10^{-4}	623	0.027	108	0.90
	2.5×10^{-4}	673	0.012	48	0.40
MnO ₂ -ZnO/MMT	2.5×10^{-4}	573	0.021	84	0.70
	2.5×10^{-4}	423	0.005	20	0.16
CeO ₂ + MnO ₂ /MMT	2.5×10^{-4}	573	0.003	12	0.10
	2.5×10^{-4}	623	0.016	64	0.53
	2.5×10^{-4}	673	0.006	24	0.20
CeO ₂ + ZnO/MMT (0.22 + 1.10) wt%	1.6×10^{-4}	573	0.006	37.5	0.20
(0.33 + 1.65) wt%	2.5×10^{-4}	573	0.25	1000	8.33
(0.44 + 2.20) wt%	3.2×10^{-4}	573	0.35	1090	11.6
(0.77 + 3.85) wt%	3.2×10^{-4}	573	0.22	687	7.33
(0.88 + 4.40) wt%	3.2×10^{-4}	573	0.08	250	2.66

^a TON = Actual moles of acetic acid formed in the reaction/ moles of active site used for reaction.

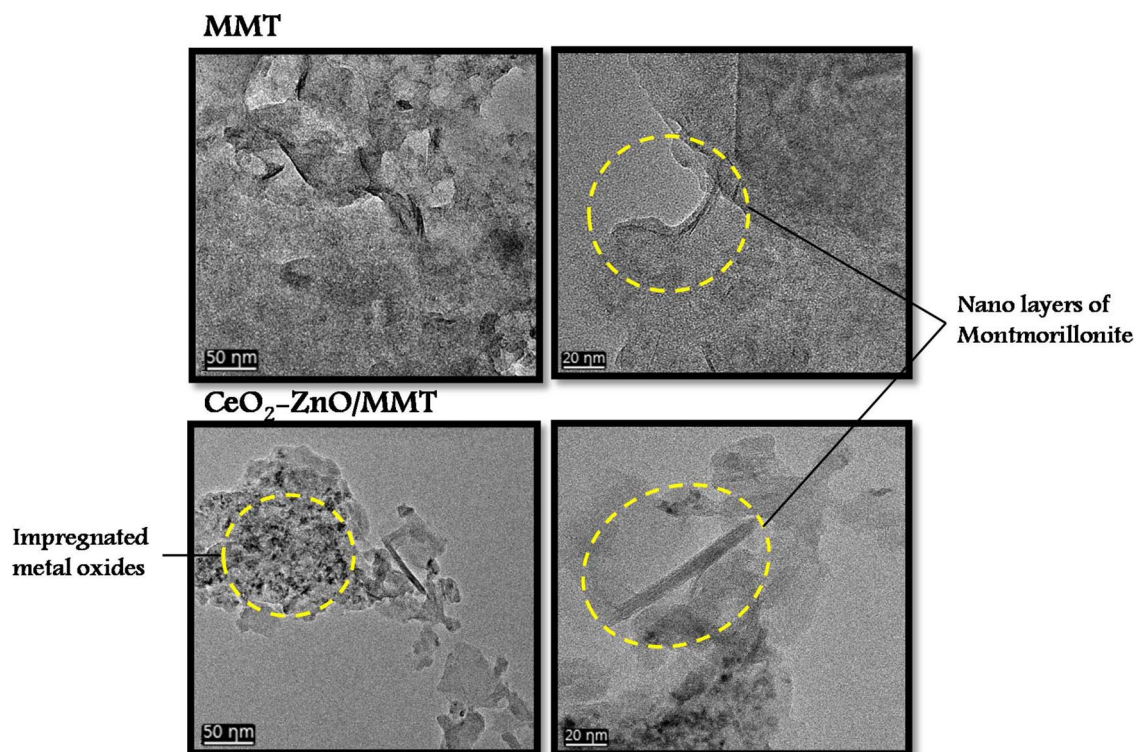


Fig. 1. Transmission electron microscopy (TEM) images for MMT and CeO₂-ZnO/MMT.

In case of CeO₂-MnO₂/MMT, the absence of Zn made its behavior completely different to the other catalysts.

We extended our work to highlight superlative activity of CeO₂-ZnO/MMT catalyst in terms of turn-over number (TON). Table 3 demonstrates the activity of few other catalysts, which are traditionally used to activate methane [22,23], under our reaction conditions. Zn-doped catalysts showed high conversion of methane with high selectivity towards acetic acid. On the other hand, silica supported heteropolyacid catalysts produced methanol as a main product due to consumption of surface oxygen of heteropolyacids [15]. Further, Cu-doped catalyst (Cu-MOR) also formed methanol in a greater concentration with a low selectivity towards acetic acid. Methane oxidizing property of Cu catalyst in this catalyst, rather than carbonylating property, might be attributed to such an observation [49]. Zn-ZSM-5, produced formic acid quantitatively and accounted highest methane conversion observed in this work. Such observation demonstrate methane activation potential of Zn doped catalysts. Over all, Zn-doped catalysts showed

good activity and especially CeO₂-ZnO/MMT performed very well showing 100% selectivity towards target acetic acid with high conversion of methane.

Further, we employed CeO₂-ZnO/MMT to study the effect of temperature by conducting the reaction at different temperatures in the range from 373 to 623 K. Maximum acetic acid formation occurred at 573 K, but at further higher temperatures, a sudden drop was found. It could be seen by TGA curves of catalysts taken at different reaction temperatures (Fig. 5). After reaction, the reactor was ice cooled and the catalyst was immediately subjected for TGA analysis. Unreacted catalyst did not show any peak corresponding to acetic acid as expected. After the reaction, however, catalysts showed a weight loss corresponding to acetic acid at around 118 °C. Another weight loss peak appearing at 425 °C could be attributed to zinc acetate. As it implying, the weight of acetic acid was increased with increase in reaction temperature from 523 to 573 K. Further increase in the reaction temperature caused a sudden decrease in weight loss of acetic acid, informing

Table 3

Comparison of catalytic activities, of other traditional catalysts employed for methane oxidation, under experimental conditions of this work.

Catalyst	Active site mmol	CH ₃ COOH (Acetic acid)		HCOOH (Formic acid)		CH ₃ OH (Methanol)		Acetic acid selectivity (%) ^b	Formic acid Selectivity (%) ^b	Methanol Selectivity (%) ^b	Methane conversion (%) ^c
		mmol	TON ^a	mmol	TON ^a	mmol	TON ^a				
20% H ₄ SiW ₁₂ O ₄₁ /SiO ₂	–	0.071	0	0.06	0	0	0	54	46	0	5.43
60% H ₄ SiW ₁₂ O ₄₁ /SiO ₂	–	0.015	0	0.02	0	0.09	0	12	16	72	4.15
Cu-MOR	0.27	0.011	0.04	0.02	0.07	0.08	0.31	9	18	73	3.68
Cu-ZSM-5	0.04	0.013	0.32	0	0	0	0	100	0	0	0.43
Zn-MOR	0.1	0.071	0.71	0.05	0.5	0	0	58	42	0	4.00
Zn-ZSM-5	0.06	0.079	1.17	0.36	5.3	0	0	18	82	0	14.57
CeO ₂ -ZnO/MMT	0.25	0.25	0.96	0	0	0	0	100	0	0	8.33

Reaction conditions: Catalyst-0.2 g, time-2 h, pressure-2 bar, temperature-573 K.

^a TON = Actual moles of acetic acid formed in the reaction/ moles of active site used for the reaction.

^b Selectivity = Moles of product formed/Total moles of product produced × 100.

^c Conversion = Total moles of product formed/Initial moles of CH₄ × 100.

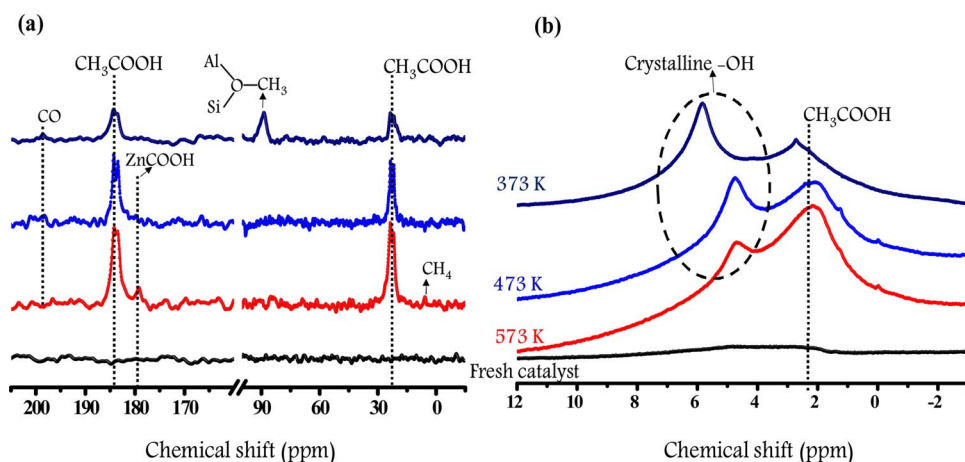


Fig. 2. Solid-state (a) ^{13}C CP/MAS and (b) ^1H CP/MAS NMR spectra taken for spent $\text{CeO}_2\text{-ZnO/MMT}$ catalyst at different temperatures. (Solid-state CP/MAS NMR was recorded on a Bruker Avance II $^+$ -400 spectrometer. For ^1H NMR instrument was operated at a rate of 400 MHz with the spin rate 13 kHz and that for ^{13}C NMR is 100 MHz and spinning rate was 8 kHz. 4 mm ZrO rotor was used for both type of analysis) Note: Data for an unreacted catalyst is provided, in each case, for comparison.

that acetic acid yield was low at higher temperatures than 573 K. This decrease might be caused by over-oxidation or the instability of acetic acid at high temperatures, in good agreement with the report by Wu et al. [23].

Solid-state ^{13}C CP NMR and ^1H CP NMR spectra taken after the reaction at different temperatures are shown in Fig. 2a and b, respectively. The spectra taken at 373 K shows characteristic peaks at 23.4 ppm, 184 ppm for $-\text{CH}_3$ and carbonyl carbon in acetic acid, respectively [23]. Another peak appearing at 179 ppm with increasing temperature can be assigned to zinc formate. A surface methoxy peak was observed at 88 ppm. In the spectra taken after the reaction at 473 and 573 K, the peak intensities are increased, indicating an increased acetic acid concentration on the catalyst surface. In ^1H NMR spectra, the characteristic acetic acid CH_3 peak was found at 2.3 ppm, and its intensity is increased with increasing temperature. The broad peak in the range 4–6 ppm, which can be assigned to crystalline $-\text{OH}$, was decreased in intensity with increasing temperature, indicating that there was greater utilization of these $-\text{OH}$ groups in producing concentrated acetic acid.

Further, to study the effects of concentration of active sites (CeO_2 and ZnO) and chemical properties of the $\text{CeO}_2\text{-ZnO/MMT}$ catalyst on the reaction, experiments were carried out by employing the catalyst prepared by varying concentration of ZnO and CeO_2 with fixed Zn/Ce ratio ($= 5$). The amount of Zn varied from 1.25 to 4.17 wt%, while that of Ce was 0.25 to 0.87 wt%. As shown in Fig. S8a, an XRD peak appears at 28.8 ppm. With the slight increase in total active site concentration, the peak sharpened. Further increment in concentration caused a peak broadening. This broadening was due to overlapping of peaks corresponding to CeO_2 and ZnO . At the peak broadening stage, it could be said that the ZnO and CeO_2 were so dispersed to provide best reaction conditions as it accounted greater yield of acetic acid. Further increase in concentration, a continued shifting of the peak towards lower theta values was observed because of composite formation among two metal oxides. The amount of acetic acid formed over catalysts prepared with different active site concentration is given in Table 2. The maximum yield was obtained with the catalyst containing 3.3 wt % Zn and 0.66 wt % Ce , that gives appropriate concentration of active sites boosting the kinetics. At higher concentrations, where the oxides form composite, the catalyst property changes completely that could cause slower kinetics in the reaction.

3.2. Mechanistic investigation in fixing favorable reaction conditions

MMT contains hydroxyl groups and has a high oxygen density, which aids CH_4 fragmentation. Ceria surfaces selectively adsorb CO_2 than ZnO [50]. On the basis of all analysis results so far, we could propose a mechanism for the co-conversion of CH_4 and CO_2 into acetic

acid over $\text{CeO}_2\text{-ZnO/MMT}$ catalyst. The mechanism contains four steps as follows.

- Step 1: Adsorption of CH_4 and CO_2 on the active sites of the catalyst.
- Step 2: Formation of intermediates (i.e., cerium carbonate and zinc methyl).
- Step 3: Migration of CO_2 to Zn-CH_3 intermediate, forming zinc acetate.
- Step 4: Formation of acetic acid and catalyst regeneration.

Research, using NMR studies, has revealed the mechanism which is informative regarding acetic acid formation on metal oxides and reduced metals doped on zeolite. However, these studies only provided mechanistic information, not accounting for reaction kinetics and the crucial catalyst properties that favors faster kinetics in acetic acid production. In this study, we have investigated each step in detail, as well as favorable reaction conditions. We focused on Langmuir-Hinshelwood concept because two different gases are being used. Our different studies revealed different mechanistic steps, with the most plausible mechanism described by those steps depicted in Fig. 3.

3.2.1. Step 1: Adsorption of CH_4 and CO_2 on active sites of the catalyst

Apparently, the Langmuir-Hinshelwood mechanism was applied using two different metal oxides to avoid adsorption competition between two gases on a single active site. CO_2 is acidic in nature and easily reacts with oxides to form carbonate. However, the feasibility of gas adsorption depends on basicity of metal oxides. Considering this concept, therefore we provided larger atomic CeO_2 sites on which CO_2 could preferably adsorb due to a high affinity [50]. The presence of oxygen vacancies also enhanced CO_2 adsorption on the catalyst. After forming cerium carbonate, the species readily undergoes reaction with the surface methyl group because the carbonate is only weakly attracted to Ce^{3+} . Although cerium carbonate is stable, the atomic size of Ce is larger, making the attractive forces between the positive nucleus and the carbonate anion weaker, resulting in faster removal of the anion from Ce atom, and thereby selectively forming acetate species. We compared the XPS (Fig. S7b) spectra of CeO_2 before and after the reaction. The spectra confirm that Ce was in +4 oxidation state, producing characteristic peaks in the range 880–920 eV. After the reaction, an additional peak clearly appeared, and peaks at 883 and 889 eV were broadened. The changes were due to the reduction of Ce^{4+} during cerium carbonate formation. The TGA (Fig. 5) curve for the sample reacted at 573 K (where the formation of acetic acid was highest) showed weight loss in the temperature range 250–300 °C due to the degradation of cerium carbonate, providing further evidence that CO_2 was attracted towards cerium to form cerium carbonate [51]. The formed surface acetate species ($\text{Zn-CH}_3\text{COO}$) are observed in solid-state ^{13}C CP/MAS NMR spectra shown in Fig. 2a. CH_4 needs high temperature to fragment because the energy required to break a C–H bond is

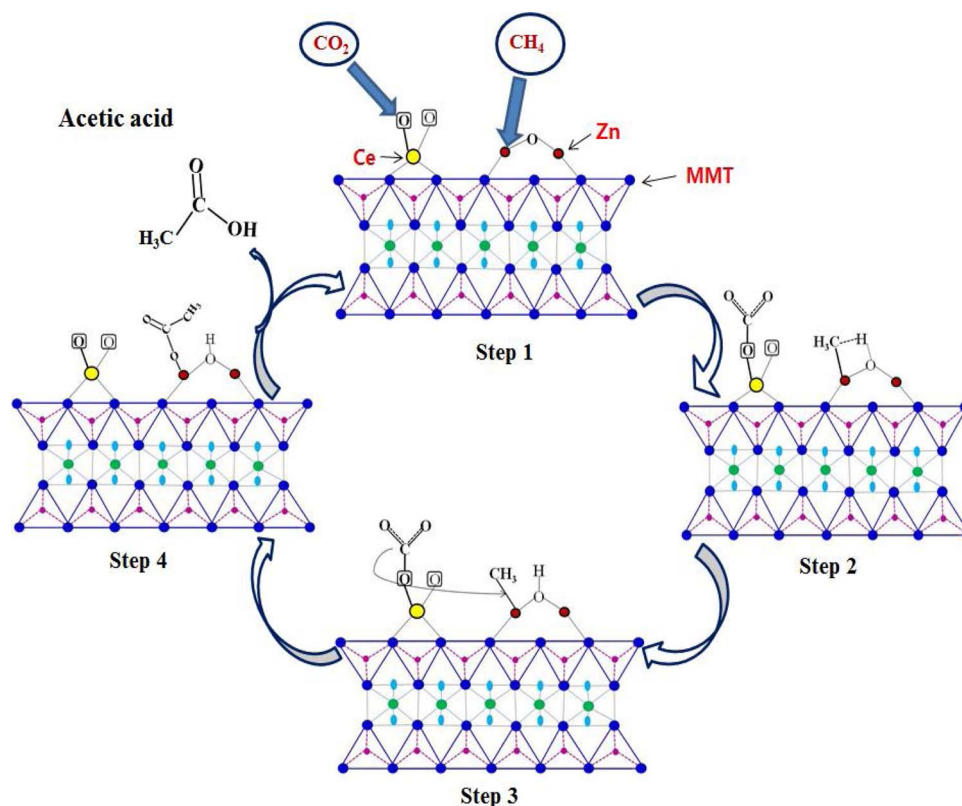


Fig. 3. Scheme of mechanistic steps involved in acetic acid formation from CH_4 and CO_2 over $\text{CeO}_2\text{-ZnO/MMT}$ catalyst.

high. However, we can enhance fragmentation by providing electron-rich surfaces (surfaces with a high oxygen density, i.e., MMT here). A higher oxygen density on MMT induces a temporary dipole between hydrogen and carbon in CH_4 through hydrogen bonding, which in turn makes the bond easy to break. However, once a methyl group has formed on the metal oxide, it must be stable to incorporate CO_2 to form acetate. A metal atom of medium atomic size and with readily available orbitals was required to allow metal methyl species to develop quickly. ZnO would provide the best site, as it meets both requirements. We

tested the adsorption preference of CH_4 by solid-state ^1H MAS NMR after purging CH_4 gas on $\text{CeO}_2\text{-ZnO/MMT}$ catalysts with different Zn concentration. As shown in Fig. 4, the catalyst with only ceria formed Ce-CH_3 groups; however, the catalyst with both metal oxides, CH_4 gas showed an affinity for zinc. As zinc concentration in the catalyst increased, the intensity of the metal methyl peak also increased with simultaneous formation of Zn-OH and Zn-CH_3 .

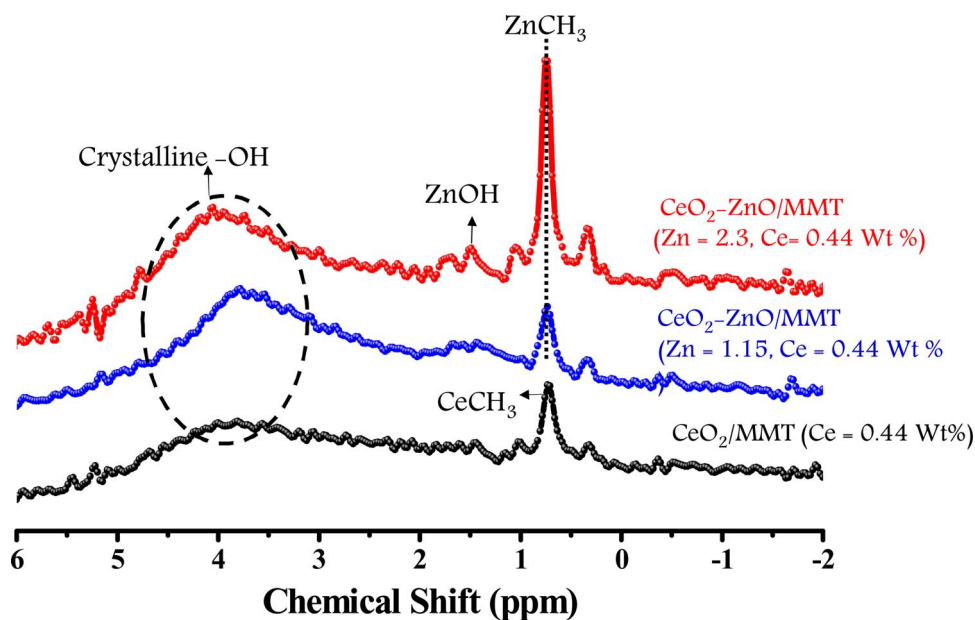


Fig. 4. Solid-state ^1H MAS NMR obtained for $\text{CeO}_2\text{-ZnO/MMT}$ (Ce = 0.44 wt%) catalysts containing varying Zn concentrations. Reaction conditions: gas, CH_4 ; pressure, 5 bars; reaction time, 2 h; catalyst amount, 0.2 g.

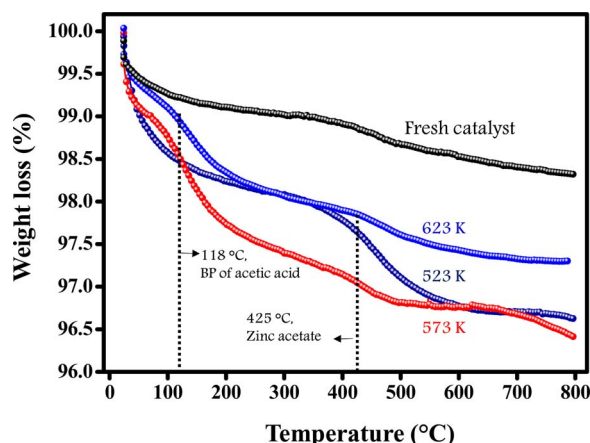


Fig. 5. TGA curves obtained from the reactions over $\text{CeO}_2\text{-ZnO/MMT}$ catalyst at different temperatures. The degradation pattern of an unreacted catalyst is provided for comparison. Reaction conditions: pressure, 8 bar; reaction time, 2 h; Catalyst amount, 0.2 g. (TGA pattern were carried out in the stream of nitrogen. The treated samples were immediately transferred to TGA panel, and experiments were performed from 25 to 800 °C with 3 °C/min heating rate.).

3.2.2. Step 2: Formation of intermediates (i.e., cerium carbonate and zinc methyl)

After adsorption of gases on different active sites, i.e., CO_2 on CeO_2 and CH_4 on ZnO , they formed their corresponding intermediates. CO_2 created carbonate after electrophilic adsorption onto cerium, while CH_4 was cleaved on Zn to form zinc methyl and zinc hydroxide. Both methyl and hydroxide forms occurred only on zinc. The simultaneous formation of zinc methyl and concurrent zinc hydroxide intermediates was confirmed by Fig. 4.

3.2.3. Step 3: Migration of CO_2 to the Zn-CH_3 intermediate to form zinc acetate

Step 3 is a key in the mechanism because the final yield depends on the migration of CO_2 . Migration of CO_2 can form different intermediates, such as $\text{CH}_3\text{COO-Zn}$, HCOO-Zn , HOOC-Zn , and $\text{CH}_3\text{OCO-Zn}$. Among them, the formation of $\text{CH}_3\text{COO-Zn}$ is energetically favored and this peak was experimentally observed in solid-state ^{13}C CP/MAS NMR (Fig. 2a). Also, in TGA curves (Fig. 5) obtained for $\text{CeO}_2\text{-ZnO/MMT}$ after reaction at different temperatures, there was a large weight loss at around 425 °C attributed to a characteristic weight loss of zinc acetate. Hence, the TGA degradation pattern proves the formation of $\text{CH}_3\text{COO-Zn}$ was energetically favored than other above mentioned intermediates. The observation is in good agreement with previous report by Zhang et al. [52].

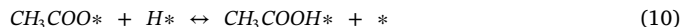
3.2.4. Step 4: Acetic acid formation and catalyst regeneration

In the final step, the formed zinc acetate abstract a proton from its surroundings to form acetic acid, detaching from the surface to leave an open site for next molecule. Readily available H^+ would increase the kinetic. In this concept, the Zn-OH formed during CH_4 activation can readily donate H^+ to the acetate group because both the acetate and proton are attached to the same metal atom. This outcome is more favored than accepting a proton from the support material. Both methods of proton donation combine to increases the rate of acetic acid formation.

4. Computational study

To obtain mechanistic insight into acetic acid formation over $\text{CeO}_2\text{-ZnO/MMT}$ catalyst, we resolved the reaction mechanism for co-conversion of CH_4 and CO_2 to form acetic acid on $\text{CeO}_2(111)$ and $\text{ZnO}(10\bar{1}0)$ surfaces via DFT calculations. Based on our experimental evidences, we investigated five elementary steps (Eq. (6)–(10)) shown

below. The asterisk (*) represents a free surface site or an adsorbed species.



Eqs. (6) and (7) indicate the adsorptions of CH_4 and CO_2 , respectively. Eq. (8) denotes the dissociation of CH_4^* to CH_3^* and H^* . Eq. (9) informs formation of CH_3COO^* formed from the bonding between CH_3^* and CO_2^* . In this step, a CO_2 molecule migrates from the original adsorption site, and get inserted into the metal-methyl bond. Finally, Eq. (10) represents the formation of CH_3COOH^* from CH_3COO^* and H^* .

We investigated the adsorption energetics and geometries of reaction intermediates on both CeO_2 and ZnO surfaces. Among the low Miller index surfaces of both oxides, we chose $\text{CeO}_2(111)$ and $\text{ZnO}(10\bar{1}0)$ surfaces as they are the most stable for the corresponding metal oxide [53–56] and are pronounced faces in the prepared catalyst as detected by XRD shown in Fig. S2a. Detail adsorption energetics and geometries of the molecular species are discussed here below. Based on these results, we discussed plausible reaction pathways for acetic acid formation over $\text{CeO}_2\text{-ZnO}$ catalyst.

4.1. Adsorption of molecular species on $\text{CeO}_2(111)$ and $\text{ZnO}(10\bar{1}0)$

We employed DFT calculations to investigate the adsorption of reaction intermediates found in co-conversion of CH_4 and CO_2 to acetic acid (CH_4 , CO_2 , CH_3 , H , CH_3COO and CH_3COOH) over $\text{CeO}_2(111)$ and $\text{ZnO}(10\bar{1}0)$ surfaces. The adsorption energetics of reaction intermediates are summarized in Table 4.

4.1.1. Adsorption of CH_4 and CO_2

CH_4 molecule adsorbs on $\text{CeO}_2(111)$ and $\text{ZnO}(10\bar{1}0)$ with the adsorption energies of -0.25 and -0.34 eV, respectively, showing that it is physisorbed on both surfaces, but more preferentially adsorbs on the ZnO surface. The CH_4 molecule is placed above 3.44 Å to the $\text{CeO}_2(111)$ while the distance between the CH_4 molecule and $\text{ZnO}(10\bar{1}0)$ is 2.79 Å. The DFT-optimized adsorption configurations are shown in Fig. 6a, b, e and f.

When CO_2 molecule is adsorbed, it forms carbonate species ($\text{CO}_3^{\delta-}$) on both surfaces by binding onto one of surface lattice oxygen atoms (Fig. 6c, d, g and h) [57]. For $\text{CeO}_2(111)$, two O atoms of CO_2 molecule are placed over the Ce atoms and the C atom in CO_2 binds on lattice oxygen of the surface, forming the carbonate species with the tilting angle from the surface normal by 40.67° . The adsorption energies of CO_2 on $\text{CeO}_2(111)$ is -0.65 eV, and the bond distance between C atom of CO_2 and surface oxygen is 1.38 Å. Meanwhile, CO_2 molecule prefers to vertically adsorb on the O atom of $\text{ZnO}(10\bar{1}0)$ with the adsorption energy of -1.08 eV. The bond distance from C atom of CO_2 to the lattice oxygen is 1.39 Å, and the two oxygen atoms of CO_2 are symmetrically located near the Zn atoms. The bond distances from the O atom of CO_2 molecule to Ce atom and Zn atoms are ~ 2.50 and ~ 2.00 Å

Table 4
Adsorption energies (eV) of reaction intermediates on $\text{CeO}_2(111)$ and $\text{ZnO}(10\bar{1}0)$.

	$\text{CeO}_2(111)$	$\text{ZnO}(10\bar{1}0)$
CH_4	-0.25	-0.34
CO_2	-0.65	-1.08
CH_3	-2.50	-1.04
H	-1.14	-0.97
CH_3COO	-1.03	-2.09
CH_3COOH	-0.79	-1.80

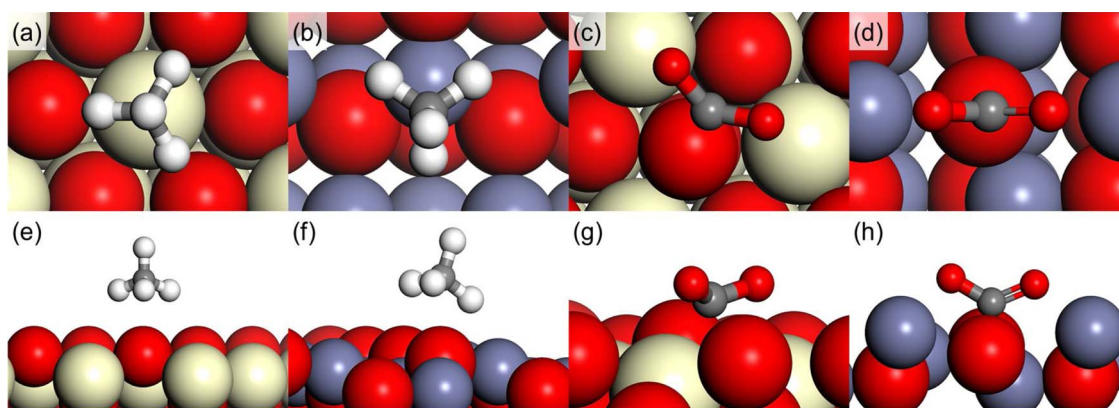


Fig. 6. DFT-optimized geometries of CH_4 and CO_2 adsorbed on $\text{CeO}_2(111)$ and $\text{ZnO}(10\bar{1}0)$. First and third columns indicate the adsorption structures of CH_4 and CO_2 on $\text{CeO}_2(111)$. Second and fourth columns show the adsorption structures of CH_4 and CO_2 on $\text{ZnO}(10\bar{1}0)$. Here, the upper and lower rows are the top and side views of each structure.

on $\text{CeO}_2(111)$ and $\text{ZnO}(10\bar{1}0)$, respectively.

4.1.2. Adsorption of CH_3 and H

As the dissociative products of CH_4 , we investigated the adsorption of CH_3 and H on $\text{CeO}_2(111)$ and $\text{ZnO}(10\bar{1}0)$. As shown in Fig. 7a, b, e and f, the CH_3 molecule adsorbs at the lattice O atom of each surface, and the bond distance between the C atom of CH_3 molecule and O atom of each surface is similar to each other. (1.43 Å for $\text{CeO}_2(111)$ and 1.45 Å for $\text{ZnO}(10\bar{1}0)$). Although their bond distances and adsorption structures are analogous, we observed the stronger adsorption of CH_3 on $\text{CeO}_2(111)$ (−2.50 eV) than that on $\text{ZnO}(10\bar{1}0)$ (−1.04 eV).

Meanwhile, the adsorbed atomic H forms the OH species by binding a surface O atom on $\text{CeO}_2(111)$ and $\text{ZnO}(10\bar{1}0)$ (Fig. 7c, d, g and h). The adsorption energies are −1.14 and −0.97 eV on $\text{CeO}_2(111)$ and $\text{ZnO}(10\bar{1}0)$, respectively. The distance between the adsorbed H and the surface lattice O is 0.97 Å for $\text{CeO}_2(111)$ and 0.98 Å for $\text{ZnO}(10\bar{1}0)$, which are similar to our DFT-calculated bond length of hydroxyl species (0.99 Å).

4.1.3. Adsorption of CH_3COO and CH_3COOH

The similar geometries are observed for CH_3COO adsorbed on both surfaces. Two O atoms of CH_3COO bind onto the two metal atoms of each surface. Here, CH_3COO molecules are tilted from the surface normal by 35.59° for $\text{CeO}_2(111)$ and 16.29° for $\text{ZnO}(10\bar{1}0)$ (Fig. 8a, b, e and f). The adsorption energy of CH_3COO on $\text{CeO}_2(111)$ is −1.03 eV and the bond distances of $\text{O}_{\text{ads}} - \text{Ce}_{\text{surf}}$ are ~2.60 Å. For $\text{ZnO}(10\bar{1}0)$, on the other hand, we found the stronger adsorption energy of CH_3COO (−2.09 eV) with shorter $\text{O}_{\text{ads}} - \text{Zn}_{\text{surf}}$ bond lengths (~1.94 Å).

In contrast, we found two different adsorption modes for CH_3COOH adsorption (Fig. 8c, d, g and h). The CH_3COOH molecule is highly tilted

away from $\text{CeO}_2(111)$ with the adsorption energy of −0.79 eV, where it is adsorbed through only one H atom in the molecule. This H atom binds onto the surface O atom with $d(\text{H}_{\text{ads}} - \text{O}_{\text{surf}})$ is 1.44 Å and the bond distance between O and H atoms of the adsorbed acetic acid is 1.07 Å. Unlike the case of adsorption on $\text{CeO}_2(111)$, when CH_3COOH is adsorbed on $\text{ZnO}(10\bar{1}0)$ with the adsorption energy of −1.80 eV, H and O atoms of the adsorbate bind to the surface O and Zn atoms, respectively. The bond distances of $\text{H}_{\text{ads}} - \text{O}_{\text{surf}}$ and $\text{O}_{\text{ads}} - \text{Zn}_{\text{surf}}$ are 1.07 and 1.90 Å, respectively. We observed the elongated adsorbate's O-H bond (1.47 Å), which was also reported in previous theoretical research [55].

4.2. Reaction pathways for co-conversion of CH_4 and CO_2 in forming acetic acid over $\text{CeO}_2(111)$ and $\text{ZnO}(10\bar{1}0)$

The reaction pathways on $\text{CeO}_2(111)$ and $\text{ZnO}(10\bar{1}0)$ were carefully examined based on the adsorption results of reaction intermediates. Since adsorbate-adsorbate interactions can be influenced by the adsorption geometries and energetics, we also considered the co-adsorption structures of reaction intermediates for each elementary step (see Table 5). In this study, we present the DFT-calculated reaction energies and activation barriers for each elementary step, as summarized in Table 5.

C–H bond cleavage in CH_4^* is exothermic on $\text{CeO}_2(111)$ (−0.81 eV) while it is slightly endothermic on $\text{ZnO}(10\bar{1}0)$ (0.06 eV) because the dissociated CH_3 and H have much stronger adsorption on $\text{CeO}_2(111)$ than $\text{ZnO}(10\bar{1}0)$ (see Table 5). For $\text{CeO}_2(111)$, CH_3 and H atoms prefer to adsorb at each different surface O atom (Fig. 9a and g). The bond distance between C atom of CH_3 and surface O atom is 1.42 Å and that between the H atom and the surface O atom is 0.97 Å. These values are almost identical to those of single adsorption of each

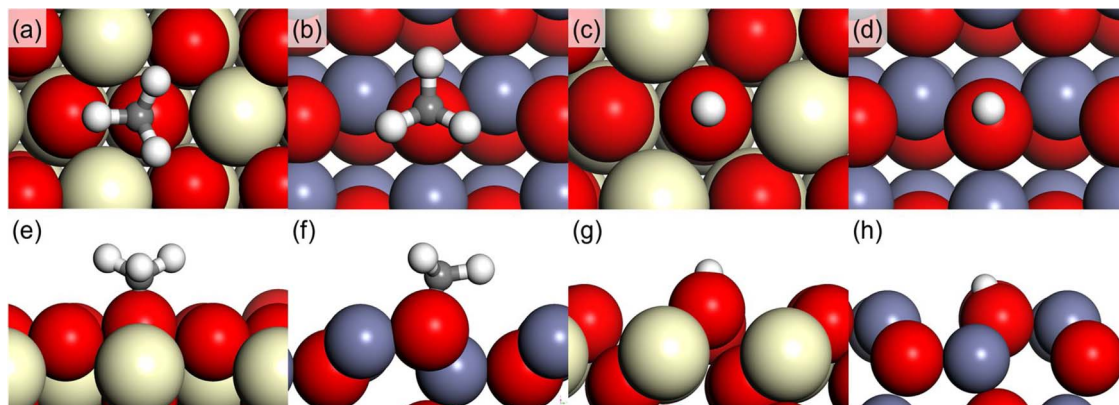


Fig. 7. DFT-optimized geometries of CH_3 and H adsorbed on $\text{CeO}_2(111)$ and $\text{ZnO}(10\bar{1}0)$. First and third columns indicate the adsorption structures of CH_3 and H on $\text{CeO}_2(111)$. Second and fourth columns indicate the adsorption structures of CH_3 and H on $\text{ZnO}(10\bar{1}0)$. Here, the upper and lower rows are the top and side views of each structure.

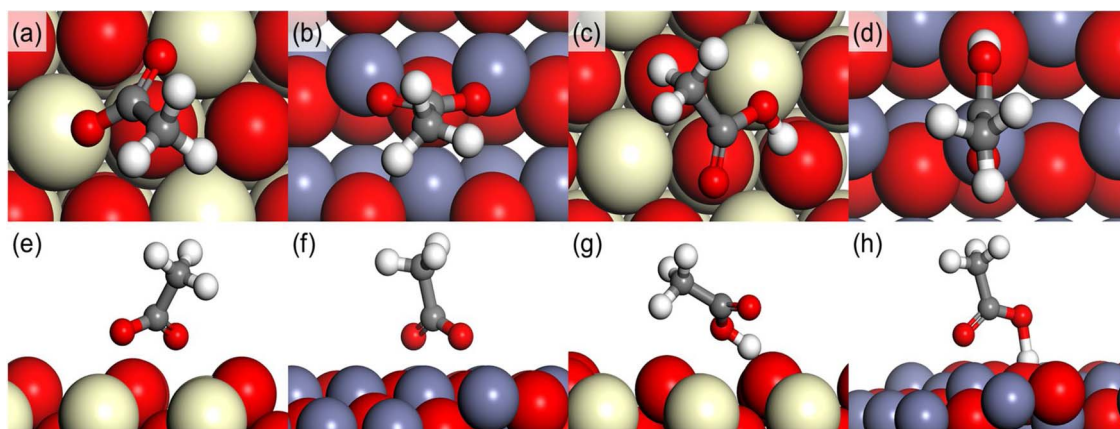


Fig. 8. DFT-optimized geometries of CH_3COO and CH_3COOH adsorbed on $\text{CeO}_2(111)$ and $\text{ZnO}(10\bar{1}0)$. First and Third columns indicate the adsorption structures of CH_3COO and CH_3COOH on $\text{CeO}_2(111)$. Second and fourth columns indicate the adsorption structures of CH_3COO and CH_3COOH on $\text{ZnO}(10\bar{1}0)$. Here, the upper and lower rows are the top and side views of each structure.

Table 5

Reaction energies (ΔE) (eV) and activation barrier (E_a) (eV) of key elementary steps on $\text{CeO}_2(111)$ and $\text{ZnO}(10\bar{1}0)$.

	$\text{CeO}_2(111)$	$\text{ZnO}(10\bar{1}0)$
	ΔE (E_a)	ΔE (E_a)
$\text{CH}_4^* + * \rightarrow \text{CH}_3^* + \text{H}^*$	−0.81 (1.33)	0.06 (0.97)
$\text{CH}_3^* + \text{CO}_2^* + \text{H}^* \rightarrow \text{CH}_3\text{COO}^* + \text{H}^* + *$	0.92 (2.83)	−1.02 (1.22)
$\text{CH}_3\text{COO}^* + \text{H}^* \rightarrow \text{CH}_3\text{COOH}^* + *$	0.48 (0.48)	0.56 (0.64)

molecule ($d(\text{C}_{\text{ads}}-\text{O}_{\text{surf}}) = 1.43 \text{ \AA}$ and $d(\text{H}_{\text{ads}}-\text{O}_{\text{surf}}) = 0.97 \text{ \AA}$). For $\text{ZnO}(10\bar{1}0)$, CH_3 alone prefers to be adsorbed onto a surface O atom (Fig. 7). In contrast, when an H atom is co-adsorbed near CH_3^* , the surface Zn atom becomes the most favorable adsorption site for CH_3 which was also identified by solid-state ^1H MAS NMR (Fig. 4) as a zinc-methyl bond while H atom is adsorbed at the nearest-neighboring surface O atom (Fig. 9b and h). The bond distance from the surface Zn atom to C atom is 1.97 \AA , and CH_3 molecule is placed on slightly away from the top region of Zn atom. The bond distance between H and surface O atom is 0.98 \AA . Contrary to the tendency from the reaction energies, the activation energy of CH_4^* dissociation on $\text{CeO}_2(111)$ (1.21 eV) is higher than that on $\text{ZnO}(10\bar{1}0)$ (0.82 eV). In this step, in order that CH_4^* physisorbed on the surface Ce atom of CeO_2 (Fig. 6a, e) is dissociated to CH_3^* and H^* (Fig. 9a and g), it should first migrate from the surface Ce atom to the surface O atom. On the other hand, the CH_4^* physisorbed on the surface Zn atom of $\text{ZnO}(10\bar{1}0)$ (Fig. 6b and f) only slightly moves from its original adsorption site during the dissociation process (Fig. 9b and h), which requires lower activation energy than that on $\text{CeO}_2(111)$.

Next, CO_2 was adsorbed on a surface O atom of $\text{CeO}_2(111)$ and $\text{ZnO}(10\bar{1}0)$, forming a carbonate species, while pre-adsorbed CH_3 and H remain in their adsorbed states (Fig. 9c, d, i and j). This step is highly

exothermic on both surfaces -0.96 eV for $\text{CeO}_2(111)$ and -0.90 eV for $\text{ZnO}(10\bar{1}0)$ without any apparent energy barriers. The bond distances between C atom of co-adsorbed CO_2 and surface O atom are unchanged as compared to those of the single adsorption of CO_2 molecule.

To form CH_3COO^* from CH_3^* and CO_2^* on the surfaces, adsorbed CO_2 molecule must migrate to a site adjacent to the methyl species. During this step, it is likely that there exists the pre-adsorbed H atom, which was originated after the CH_4 dissociation, on the surfaces near the CH_3^* , CO_2^* and CH_3COO^* . If we only considered CH_3^* and CO_2^* as initial species and CH_3COO^* as a final species without pre-adsorbed H in this step, $\text{CH}_3^* + \text{CO}_2^* \rightarrow \text{CH}_3\text{COO}^*$, CH_3COO^* formation is strongly endothermic on $\text{CeO}_2(111)$ (2.26 eV), representing the largest endothermicity in the entire reaction, whereas it is slightly exothermic on $\text{ZnO}(10\bar{1}0)$ (-0.01 eV). On the other hand, to elucidate the effect of pre-adsorbed H atom, we additionally calculated the energetics for the following reaction, $\text{CH}_3^* + \text{CO}_2^* + \text{H}^* \rightarrow \text{CH}_3\text{COO}^* + \text{H}^*$. The adsorption geometries of the initial state ($\text{CH}_3^* + \text{CO}_2^* + \text{H}^*$) on $\text{CeO}_2(111)$ is almost identical with the case of adsorption without H^* (Fig. 9c and i). However, we found that the adsorption strength of CH_3 with pre-adsorbed H on $\text{ZnO}(10\bar{1}0)$ is stronger than without H^* , where the bond distance between C atom of the adsorbed CH_3 and surface Zn atom is shortened by 0.25 \AA . Meanwhile, the adsorption strength of CO_2 molecules on $\text{ZnO}(10\bar{1}0)$ is barely changed upon the pre-adsorbed H (Fig. 9d and j). In case of the final state, the adsorbed CH_3COO molecules without H^* are tilted away from the surface normal and their two oxygen atoms are located above the surface metal atoms (Fig. 8a, b, e, and f). However, introducing the pre-adsorbed H makes CH_3COO^* upright on $\text{CeO}_2(111)$ (Fig. 9e and k) as H^* atom is adsorbed at the nearest-neighboring surface O atom. On the other hand, CH_3COO^* remains its tilting angle on $\text{ZnO}(10\bar{1}0)$, but the one of O atom of CH_3COO slightly move toward the adsorbed hydrogen due to the attractive force between them (Fig. 9f and l). Under the circumstance with pre-

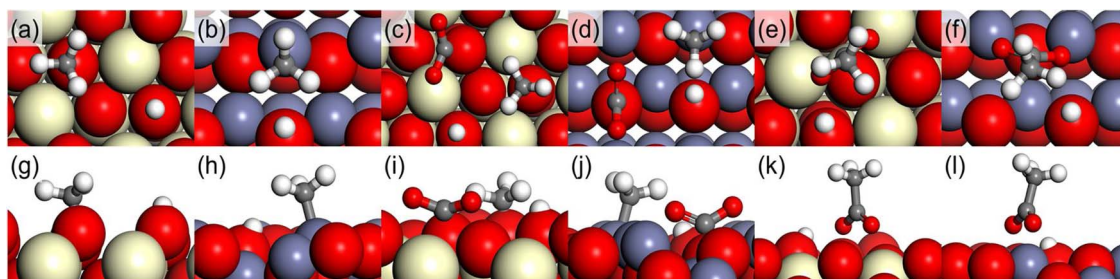


Fig. 9. DFT-optimized geometries of CH_3 , co-adsorbed CH_3 and CO_2 , CH_3COO adsorbed on H-preadsorbed on $\text{CeO}_2(111)$ and $\text{ZnO}(10\bar{1}0)$. First, third and fifth columns indicate the adsorption structures of CH_3 , co-adsorbed CH_3 and CO_2 , CH_3COO on H-preadsorbed $\text{CeO}_2(111)$. Second, fourth and sixth columns indicate the adsorption structures of CH_3 , co-adsorbed CH_3 and CO_2 , CH_3COO on H-preadsorbed $\text{ZnO}(10\bar{1}0)$. Here, the upper and lower rows are the top and side views of each structure.

adsorbed H, the reaction energies for CH_3COO^* formation are significantly reduced to 0.92 and -1.02 eV for $\text{CeO}_2(111)$ and $\text{ZnO}(10\bar{1}0)$, respectively, which implies that the pre-adsorbed H atom assists CH_3COO^* formation on both surfaces. In this regard, we will only take into account the adsorption energetics with the pre-adsorbed H atom for further discussion.

Based on the results, it is found that in this elementary step, the reaction energies between two surfaces is dramatically different – endothermicity of 0.92 eV for CeO_2 and exothermicity of -1.02 eV for ZnO . Furthermore, $\text{CeO}_2(111)$ has an activation barrier of 2.83 eV while $\text{ZnO}(10\bar{1}0)$ has that of 1.22 eV, which indicates that acetate formation is highly favored on $\text{ZnO}(10\bar{1}0)$ rather than $\text{CeO}_2(111)$. This CO_2 insertion step into CH_3 is a rate-determining step of the entire reaction for both surfaces. For ZnO surface, we additionally investigated the possibility of further dehydrogenation of the adsorbed CH_3 species. This is important because if the dehydrogenation of CH_3 is preferred, the reaction would result in the different products. Thus, we computed the activation energy for CH_3^* dehydrogenation on $\text{ZnO}(10\bar{1}0)$ to compare this with the activation energy for acetate formation. Our results show that the activation energy of dehydrogenation (1.81 eV) is much larger than that of acetate formation (1.22 eV) on $\text{ZnO}(10\bar{1}0)$, which indicates that the ZnO surface stabilizes the CH_3 species that can further experience C–C coupling reaction (CO_2 insertion into CH_3) to form acetate rather than CH_3 dehydrogenation.

Finally, when CH_3COO^* uptakes the surface H^* atom to form CH_3COOH^* , the endothermic reaction energies are found to be 0.48 and 0.56 eV for $\text{CeO}_2(111)$ and $\text{ZnO}(10\bar{1}0)$, respectively. The activation barriers at this elementary step are 0.48 (that is same as the reaction energy) and 0.64 eV for $\text{CeO}_2(111)$ and $\text{ZnO}(10\bar{1}0)$, respectively. For $\text{CeO}_2(111)$, CH_3COOH^* is tilted again after the formation, weakly binding onto the surface O atom through only one of H atom in the molecule (Fig. 8c and g). Unlikely, CH_3COOH^* binds onto the surface O and Zn atoms of $\text{ZnO}(10\bar{1}0)$ through the H and O atoms in the molecule, respectively, rotating 90° from the adsorption geometry of CH_3COO^* (Fig. 8d and h).

To summarize our DFT results, we plotted the entire energy profile (Fig. 10) of acetic acid formation reaction, which shows that the reaction is more favorable on $\text{ZnO}(10\bar{1}0)$ than $\text{CeO}_2(111)$. For CH_4^* dissociation step, the activation barrier on $\text{CeO}_2(111)$ is higher than that on $\text{ZnO}(10\bar{1}0)$, indicating that the CH_4^* can be dissociated more readily on $\text{ZnO}(10\bar{1}0)$. The CO_2 adsorption step exhibits no energy barriers for both $\text{CeO}_2(111)$ and $\text{ZnO}(10\bar{1}0)$. At the CO_2 insertion step into CH_3 ,

CH_3COO^* formation is kinetically more preferred on $\text{ZnO}(10\bar{1}0)$ than $\text{CeO}_2(111)$. Lastly, for CH_3COOH^* formation, we observed moderate activation barriers which are lower than those at the rate-determining step (CH_3COO^* formation) for each surface. We therefore conclude that the acetic acid formation is much easier on ZnO catalyst than CeO_2 , which is in good agreement with our experimental results (Table 2).

In this respect, for the $\text{CeO}_2\text{-ZnO/MMT}$ catalyst, the active site (Zn side) assists the CH_3COO^* formation, which has the largest energy barrier for co-conversion of CH_4 and CO_2 to acetic acid on the Ce side. This causes the enhanced catalytic conversion to acetic acid observed for the $\text{CeO}_2\text{-ZnO/MMT}$ catalyst. Furthermore, during acetate formation step on this catalyst, it is also important to consider the migration of CO_2 from one metal oxide to the other. The diffusion barrier has often been approximated from the difference in adsorption energies at initial and final adsorption sites, which allows us to easily understand the surface diffusion of an adsorbed molecule on the catalyst surfaces [53–56,58–63]. Recently, Andersen et al., reported the effectiveness of dual active sites by introducing such the thermodynamic diffusion barrier between the two monofunctional catalysts [61]. Here, we employed this concept to provide insight for the direction of migration on $\text{CeO}_2\text{-ZnO/MMT}$ catalyst. The migration of adsorbed CO_2 from $\text{CeO}_2(111)$ to $\text{ZnO}(10\bar{1}0)$ was energetically exothermic (-0.43 eV) while that of opposite direction was endothermic. The favorable migration tendency from CeO_2 to ZnO also accelerates the formation of acetate on Zn side, thus explaining our experimental results. It is noteworthy that our DFT calculations were performed at the zero kelvin temperature. In order to precisely consider the effect of temperature, it may be necessary to employ Gibbs free energies in our energy diagram or develop the microkinetic modeling. However, since the entropies of adsorbed species on the surfaces are negligible, temperature contribution (TAS) to the Gibbs free energies of the surface reaction would be small [64]. Thus, the effect of temperature is not significant for the activation energies of the surface reaction (Eq. (8)–(9)). On the other hand, the TAS term for the desorption process of acetic acid would have a positive value so that it can assist the desorption of acetic acid from the surface by lowering the Gibbs free energy ($\Delta G = \Delta E_{\text{des}} - \text{TAS}$). It is therefore expected that the rate of acetic acid formation would be more increased at the real experimental temperature (573 K). However, it does not change our main conclusion that CO_2 is easier to migrate from CeO_2 to the ZnO side and the formation of acetic acid is also strongly favored on ZnO catalyst.

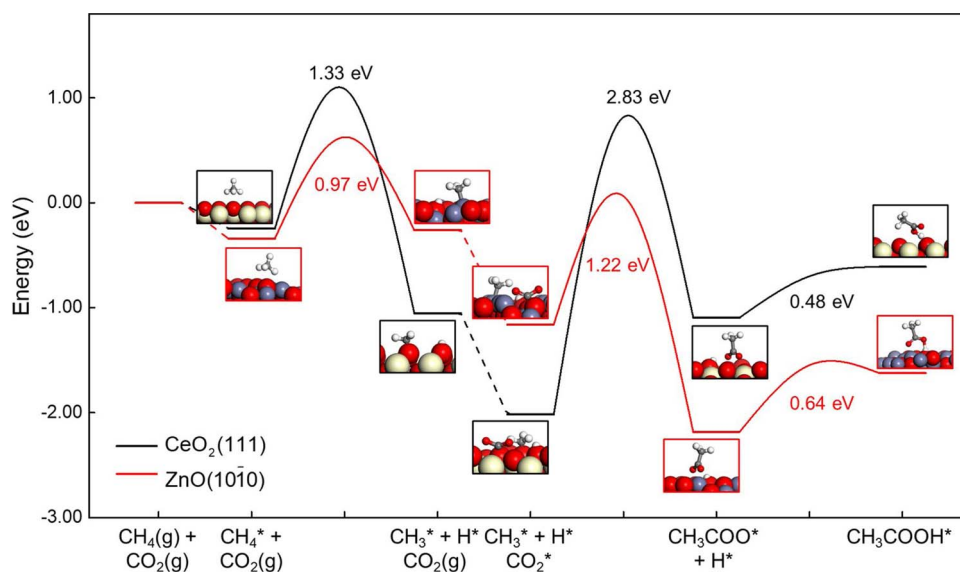


Fig. 10. Energy profiles of acetic acid formation on $\text{CeO}_2(111)$ and $\text{ZnO}(10\bar{1}0)$. Black and red lines indicate the reaction pathways on $\text{CeO}_2(111)$ and $\text{ZnO}(10\bar{1}0)$, respectively. (For interpretation of the references to colour in this figure legend, the reader is referred to the web version of this article).

5. Conclusions

Direct co-conversion of CH₄ and CO₂ into acetic acid was conducted over MMT supported single and dual active site catalysts having ZnO, MnO₂, and CeO₂. In particular, ZnO/MMT performed well among single active site catalyst with 0.055 mmol of acetic acid production. Dual active site catalysts solved the surface adsorption competition of reactant gases and maximized the acetic acid yield. Among the dual active site catalysts, CeO₂-ZnO/MMT showed the best catalytic activity in terms of acetic acid yield (0.35 mmol) followed by MnO₂-ZnO/MMT and CeO₂-MnO₂/MMT. Hence the varying atomic size of active site, and the presence of Lewis acid ZnO in the catalyst, have a significant role in surface carbonylation reaction of CH₄. This was further confirmed by DFT study on CeO₂(111) and ZnO(10 $\bar{1}$ 0) faces that ZnO promotes the formation of surface acetate by means of CO₂ migration from bigger size CeO₂ onto the ZnO. Additionally, XRD and DFT studies collectively depicted that the concentration of active site and distance between them over MMT support will take important role in reaction kinetics. Experimental results showed that the presence of Ce: 0.44 wt%, and Zn: 2.20 wt%, which accounts minimal distance between those two species over MMT, could boost the reaction kinetics. In order to increase the acetic acid yield further, a research is on-going for controlling the distance between the active sites.

Acknowledgements

This work was supported by the Energy Efficiency & Resources (No. 20163010092210) of the Korea Institute of Energy Technology Evaluation and Planning (KETEP) grant funded by the Korea government Ministry of Trade, Industry & Energy. This work was also supported by the C1 Gas Refinery Program through the National Research Foundation of Korea (NRF) funded by the Ministry of Science and ICT (2015M3D3A1A01064899).

Appendix A. Supplementary data

Supplementary material related to this article can be found, in the online version, at doi:<https://doi.org/10.1016/j.apcatb.2018.01.058>.

References

- J. Qin, S. Wang, X. Wang, Visible-light reduction CO₂ with dodecahedral zeolitic imidazolate framework ZIF-67 as an efficient co-catalyst, *Appl. Catal. B Environ.* 209 (2017) 476–482, <http://dx.doi.org/10.1016/j.apcatb.2017.03.018>.
- W. Taifan, J. Baltrusaitis, CH₄ conversion to value added products: potential, limitations and extensions of a single step heterogeneous catalysis, *Appl. Catal. B Environ.* 198 (2016) 525–547, <http://dx.doi.org/10.1016/j.apcatb.2016.05.081>.
- K. Villa, S. Murcia-López, J.R. Morante, T. Andreu, An insight on the role of La in mesoporous WO₃ for the photocatalytic conversion of methane into methanol, *Appl. Catal. B Environ.* 187 (2016) 30–36, <http://dx.doi.org/10.1016/j.apcatb.2016.01.032>.
- R. Pang, K. Teramura, H. Asakura, S. Hosokawa, T. Tanaka, Highly selective photocatalytic conversion of CO₂ by water over Ag-loaded SrNb₂O₆ nanorods, *Appl. Catal. B Environ.* 218 (2017) 770–778, <http://dx.doi.org/10.1016/j.apcatb.2017.06.052>.
- Q. Shen, J. Ma, X. Huang, N. Yang, G. Zhao, Enhanced carbon dioxide conversion to formate on a multi-functional synergistic photoelectrocatalytic interface, *Appl. Catal. B Environ.* 219 (2017) 45–52, <http://dx.doi.org/10.1016/j.apcatb.2017.07.029>.
- A. Solis-Garcia, J.F. Louvier-Hernandez, A. Almendarez-Camarillo, J.C. Fierro-Gonzalez, Participation of surface bicarbonate, formate and methoxy species in the carbon dioxide methanation catalyzed by ZrO₂-supported Ni, *Appl. Catal. B Environ.* 218 (2017) 611–620, <http://dx.doi.org/10.1016/j.apcatb.2017.06.063>.
- D. Mei, X. Zhu, C. Wu, B. Ashford, P.T. Williams, X. Tu, Plasma-photocatalytic conversion of CO₂ at low temperatures: understanding the synergistic effect of plasma-catalysis, *Appl. Catal. B Environ.* 182 (2016) 525–532, <http://dx.doi.org/10.1016/j.apcatb.2015.09.052>.
- J. Sentek, K. Krawczyk, M. Mhotek, M. Kalczyńska, T. Kroker, T. Kolb, A. Schenk, K.-H. Gericke, K. Schmidt-Szalowski, Plasma-catalytic methane conversion with carbon dioxide in dielectric barrier discharges, *Appl. Catal. B Environ.* 94 (2010) 19–26, <http://dx.doi.org/10.1016/j.apcatb.2009.10.016>.
- S. Wannakao, C. Warakulwit, K. Kongpatpanich, M. Probst, J. Limtrakul, Methane activation in gold cation-exchanged zeolites: a DFT study, *ACS Catal.* 2 (2012) 986–992, <http://dx.doi.org/10.1021/cs200653q>.
- R. Shavi, V. Hiremath, A. Sharma, S.O. Won, J.G. Seo, Synergistic activating effect of promoter and oxidant in single step conversion of methane into methanol over a tailored polymer-Ag coordination complex, *RSC Adv.* 7 (2017) 24168–24176, <http://dx.doi.org/10.1039/C7RA02700A>.
- A.A. Gabrienko, S.S. Arzumano, M.V. Luzgin, A.G. Stepanov, V.N. Parmon, Methane activation on Zn²⁺-exchanged ZSM-5 zeolites. The effect of molecular oxygen addition, *J. Phys. Chem. C* 119 (2015) 24910–24918, <http://dx.doi.org/10.1021/acs.jpcc.5b08759>.
- R. Shavi, V. Hiremath, J.G. Seo, Radical-initiated oxidative conversion of methane to methanol over metallic iron and copper catalysts, *Mol. Catal.* 445 (2018) 232–239, <http://dx.doi.org/10.1016/j.mcat.2017.12.001>.
- Y. Taniguchi, T. Hayashida, H. Shibasaki, D. Piao, T. Kitamura, T. Yamaji, Y. Fujiwara, Highly efficient vanadium-catalyzed transformation of CH₄ and CO to acetic acid, *Org. Lett.* 1 (1999) 557–560, <http://dx.doi.org/10.1021/ol990073r>.
- A. Phan, A.U. Czaja, F. Gándara, C.B. Knobler, O.M. Yaghi, Metal-organic frameworks of vanadium as catalysts for conversion of methane to acetic acid, *Inorg. Chem.* 50 (2011) 7388–7390, <http://dx.doi.org/10.1021/ic201396m>.
- M. Sun, E. Abou-Hamad, A.J. Rossini, J. Zhang, A. Lesage, H. Zhu, J. Pelletier, L. Emsley, V. Caps, J.-M. Basset, Methane reacts with heteropolyacids chemisorbed on silica to produce acetic acid under soft conditions, *J. Am. Chem. Soc.* 135 (2013) 804–810, <http://dx.doi.org/10.1021/ja309966j>.
- E.M. Wilcox, G.W. Roberts, J.J. Spivey, Direct catalytic formation of acetic acid from CO₂ and methane, *Catal. Today* 88 (2003) 83–90, <http://dx.doi.org/10.1016/j.cattod.2003.08.007>.
- Y.-H. Ding, W. Huang, Y.-G. Wang, Direct synthesis of acetic acid from CH₄ and CO₂ by a step-wise route over Pd/SiO₂ and Rh/SiO₂ catalysts, *Fuel Process. Technol.* 88 (2007) 319–324, <http://dx.doi.org/10.1016/j.fuproc.2004.09.003>.
- I.H. Hristov, T. Ziegler, Density functional theory study of the direct conversion of methane to acetic acid by RhCl₃, *Organometallics* 102 (2003) 3513–3525, <http://dx.doi.org/10.1021/om030217c>.
- S. Chempath, A.T. Bell, Density functional theory analysis of the reaction pathway for methane oxidation to acetic acid catalyzed by Pd²⁺ in sulfuric acid, *J. Am. Chem. Soc.* (2006) 4650–4657, <http://dx.doi.org/10.1021/ja055756i>.
- X. Zhao, R. Zhang, Q. Wang, D. Li, B. Wang, L. Ling, Source and major species of CH_x (x = 1–3) in acetic acid synthesis from methane-syngas on Rh catalyst: a theoretical study, *RSC Adv.* 4 (2014) 58631–58642, <http://dx.doi.org/10.1039/C4RA05591H>.
- M.V. Kirillova, M.L. Kuznetsov, P.M. Reis, J.A.L. Da Silva, J.J.R. Fraústo Da Silva, A.J.L. Pombeiro, Direct and remarkably efficient conversion of methane into acetic acid catalyzed by amavadin and related vanadium complexes. A synthetic and a theoretical DFT mechanistic study, *J. Am. Chem. Soc.* 129 (2007) 10531–10545, <http://dx.doi.org/10.1021/ja072531u>.
- K. Narsimhan, V.K. Michaelis, G. Mathies, W.R. Gunther, R.G. Griffin, Y. Román-Leshkov, Methane to acetic acid over Cu-exchanged zeolites: mechanistic insights from a site-specific carbonylation reaction, *J. Am. Chem. Soc.* 137 (2015) 1825–1832, <http://dx.doi.org/10.1021/ja5106927>.
- J.-F. Wu, S.-M. Yu, W.D. Wang, Y.-X. Fan, S. Bai, C.-W. Zhang, Q. Gao, J. Huang, W. Wang, Mechanistic insight into the formation of acetic acid from the direct conversion of methane and carbon dioxide on zinc-modified H-ZSM-5 zeolite, *J. Am. Chem. Soc.* 135 (2013) 13567–13573, <http://dx.doi.org/10.1021/ja406978q>.
- B.D. Montejo-Valencia, Y.J. Pagán-Torres, M.M. Martínez-Liñeira, M.C. Curet-Arana, Density functional theory (DFT) study to unravel the catalytic properties of M-exchanged MFI, (M = Be, Co, Cu, Mg, Mn, Zn) for the conversion of methane and carbon dioxide to acetic acid, *ACS Catal.* 7 (2017) 6719–6728, <http://dx.doi.org/10.1021/acscatal.7b00844>.
- W. Panjan, J. Sirirajarensre, C. Warakulwit, P. Pantu, J. Limtrakul, The conversion of CO₂ and CH₄ to acetic acid over the Au-exchanged ZSM-5 catalyst: a density functional theory study, *Phys. Chem. Chem. Phys.* 14 (2012) 16588, <http://dx.doi.org/10.1039/c2cp42066j>.
- Y. Zhao, C. Cui, J. Han, H. Wang, X. Zhu, Q. Ge, Direct C-C coupling of CO₂ and the methyl group from CH₄ activation through facile insertion of CO₂ into Zn-CH₃ σ-bond, *J. Am. Chem. Soc.* 138 (2016) 10191–10198, <http://dx.doi.org/10.1021/jacs.6b04446>.
- A.M. Rabie, M.A. Betiha, S.-E. Park, Direct synthesis of acetic acid by simultaneous co-activation of methane and CO₂ over Cu-exchanged ZSM-5 catalysts, *Appl. Catal. B Environ.* 215 (2017) 50–59, <http://dx.doi.org/10.1016/j.apcatb.2017.05.053>.
- X. Weng, H. Ren, M. Chen, H. Wan, Effect of surface oxygen on the activation of methane on palladium and platinum surfaces, *ACS Catal.* 4 (2014) 2598–2604, <http://dx.doi.org/10.1021/cs500510x>.
- Y. Zhao, C. Cui, J. Han, H. Wang, X. Zhu, Q. Ge, Direct C-C coupling of CO₂ and the methyl group from CH₄ activation through facile insertion of CO₂ into Zn-CH₃ σ-bond, *J. Am. Chem. Soc.* 138 (2016) 10191–10198, <http://dx.doi.org/10.1021/jacs.6b04446>.
- G. Kresse, J. Hafner, Ab initio molecular dynamics for liquid metals, *Phys. Rev. B* 47 (1993) 558–561, <http://dx.doi.org/10.1103/PhysRevB.47.558>.
- G. Kresse, J. Furthmüller, Efficient iterative schemes for ab initio total-energy calculations using a plane-wave basis set, *Phys. Rev. B* 54 (1996) 11169–11186, <http://dx.doi.org/10.1103/PhysRevB.54.11169>.
- G. Kresse, J. Hafner, Norm-conserving and ultrasoft pseudopotentials for first-row and transition elements, *J. Phys. Condens. Matter* 6 (1994) 8245–8257, <http://dx.doi.org/10.1088/0953-8984/6/40/015>.
- D.S. Sholl, J.A. Steckel, Density functional theory: a practical introduction, Chapter 01, *Density Funct. Theory A Pract. Intro.* (2009), pp. 1–33, <http://dx.doi.org/10.1002/9780470447710.ch1>.
- J.P. Perdew, K. Burke, M. Ernzerhof, Generalized gradient approximation made

- simple, *Phys. Rev. Lett.* 77 (1996) 3865–3868, <http://dx.doi.org/10.1103/PhysRevLett.77.3865>.
- [35] S. Grimme, J. Antony, S. Ehrlich, H. Krieg, A consistent and accurate ab initio parametrization of density functional dispersion correction (DFT-D) for the 94 elements H–Pu, *J. Chem. Phys.* 132 (2010) 154104, <http://dx.doi.org/10.1063/1.3382344>.
- [36] M. Methfessel, A.T. Paxton, High-precision sampling for Brillouin-zone integration in metals, *Phys. Rev. B* 40 (1989) 3616–3621, <http://dx.doi.org/10.1103/PhysRevB.40.3616>.
- [37] L. Bengtsson, Dipole correction for surface supercell calculations, *Phys. Rev. B* 59 (1999) 12301–12304, <http://dx.doi.org/10.1103/PhysRevB.59.12301>.
- [38] J. Neugebauer, M. Scheffler, Adsorbate-substrate and adsorbate-adsorbate interactions of Na and K adlayers on Al(111), *Phys. Rev. B* 46 (1992) 16067–16080, <http://dx.doi.org/10.1103/PhysRevB.46.16067>.
- [39] S. Zhao, L. Ling, B. Wang, R. Zhang, D. Li, Q. Wang, J. Wang, Theoretic insight into the desulfurization mechanism: removal of H₂S by Ceria (110), *J. Phys. Chem. C* 119 (2015) 7678–7688, <http://dx.doi.org/10.1021/jp511289k>.
- [40] M. Nolan, S.C. Parker, G.W. Watson, The electronic structure of oxygen vacancy defects at the low index surfaces of ceria, *Surf. Sci.* 595 (2005) 223–232, <http://dx.doi.org/10.1016/j.susc.2005.08.015>.
- [41] D. Fernández-Torre, J. Carrasco, M.V. Ganduglia-Pirovano, R. Pérez, Hydrogen activation, diffusion, and clustering on CeO₂(111): a DFT + U study, *J. Chem. Phys.* 141 (2014) 14703, <http://dx.doi.org/10.1063/1.4885546>.
- [42] J.L.F. Da Silva, M.V. Ganduglia-Pirovano, J. Sauer, V. Bayer, G. Kresse, Hybrid functionals applied to rare-earth oxides: the example of ceria, *Phys. Rev. B* 75 (2007) 45121, <http://dx.doi.org/10.1103/PhysRevB.75.045121>.
- [43] G.-Y. Huang, C.-Y. Wang, J.-T. Wang, Detailed check of the LDA + U and GGA + U corrected method for defect calculations in wurtzite ZnO, *Comput. Phys. Commun.* 183 (2012) 1749–1752, <http://dx.doi.org/10.1016/j.cpc.2012.03.017>.
- [44] M.K. Yaakob, N.H. Hussin, M.F.M. Taib, T.I.T. Kudin, O.H. Hassan, A.M.M. Ali, M.Z.A. Yahya, First principles LDA + U calculations for ZnO materials, *Integr. Ferroelectr.* 155 (2014) 15–22, <http://dx.doi.org/10.1080/10584587.2014.905086>.
- [45] D. İuşan, M. Kabir, O. Grånäs, O. Eriksson, B. Sanyal, Microscopic picture of Co clustering in ZnO, *Phys. Rev. B* 79 (2009) 125202, <http://dx.doi.org/10.1103/PhysRevB.79.125202>.
- [46] E. Kümmerle, G. Heger, The structures of C–Ce₂O_{3+δ}, Ce₇O₁₂, and Ce₁₁O₂₀, *J. Solid State Chem.* 147 (1999) 485–500, <http://dx.doi.org/10.1006/jssc.1999.8403>.
- [47] F. Decremps, F. Datchi, A.M. Saitta, A. Polian, S. Pascarelli, A. Di Cicco, J.P. Itié, F. Baudelet, Local structure of condensed zinc oxide, *Phys. Rev. B* 68 (2003) 104101, <http://dx.doi.org/10.1103/PhysRevB.68.104101>.
- [48] G. Henkelman, B.P. Uberuaga, H. Jónsson, A climbing image nudged elastic band method for finding saddle points and minimum energy paths, *J. Chem. Phys.* 113 (2000) 9901–9904, <http://dx.doi.org/10.1063/1.1329672>.
- [49] S. Grundner, M.A.C. Markovits, G. Li, M. Tromp, E.A. Pidko, E.J.M. Hensen, A. Jentys, M. Sanchez-Sanchez, J.A. Lercher, Single-site trinuclear copper oxygen clusters in mordenite for selective conversion of methane to methanol, *Nat. Commun.* 6 (2015) 7546, <http://dx.doi.org/10.1038/ncomms8546>.
- [50] K.R. Hahn, M. Iannuzzi, A.P. Seitsonen, J. Hutter, Coverage effect of the CO₂ adsorption mechanisms on CeO₂(111) by first principles analysis, *J. Phys. Chem. C* 117 (2013) 1701–1711, <http://dx.doi.org/10.1021/jp309565u>.
- [51] C.-C. Liu, C.-Y. Mou, S.S.-F. Yu, S.I. Chan, Heterogeneous formulation of the tri-copper complex for efficient catalytic conversion of methane into methanol at ambient temperature and pressure, *Energy Environ. Sci.* 9 (2016) 1361–1374, <http://dx.doi.org/10.1039/C5EE03372A>.
- [52] R. Zhang, L. Song, H. Liu, B. Wang, The interaction mechanism of CO₂ with CH₃ and H on Cu (111) surface in synthesis of acetic acid from CH₄/CO₂: a DFT study, *Appl. Catal. A Gen.* 443–444 (2012) 50–58, <http://dx.doi.org/10.1016/j.apcata.2012.07.024>.
- [53] D. Knapp, T. Ziegler, Methane dissociation on the Ceria (111) surface, *J. Phys. Chem. C* 112 (2008) 17311–17318, <http://dx.doi.org/10.1021/jp8039862>.
- [54] Z. Yang, T.K. Woo, M. Baudin, K. Hermansson, Atomic and electronic structure of unreduced and reduced CeO₂ surfaces: a first-principles study, *J. Chem. Phys.* 120 (2004) 7741–7749, <http://dx.doi.org/10.1063/1.1688316>.
- [55] J. Chang, R. Ahmed, H. Wang, H. Liu, R. Li, P. Wang, E.R. Wacławik, ZnO nanowires with high-index {101 $\bar{1}$ } facets for enhanced energy conversion efficiency of dye-sensitized solar cells, *J. Phys. Chem. C* 117 (2013) 13836–13844, <http://dx.doi.org/10.1021/jp402742n>.
- [56] A. Dominguez, M. Lorke, A.L. Schoenhalz, A.L. Rosa, T. Frauenheim, A.R. Rocha, G.M. Dalpian, First principles investigations on the electronic structure of anchor groups on ZnO nanowires and surfaces, *J. Appl. Phys.* 115 (2014), <http://dx.doi.org/10.1063/1.4879676>.
- [57] K. Kim, J.W. Han, Mechanistic study for enhanced CO oxidation activity on (Mn, Fe) co-doped CeO₂ (111), *Catal. Today* 293–294 (2017) 82–88, <http://dx.doi.org/10.1016/j.cattod.2016.11.046>.
- [58] A. Herron, J. Scaranto, P. Ferrin, S. Li, M. Mavrikakis, Trends in formic acid decomposition on model transition metal surfaces: a density functional theory study, *ACS Catal.* 4 (2014) 4434–4445, <http://dx.doi.org/10.1021/cs500737p>.
- [59] G. Jones, T. Bligaard, F. Abild-Pedersen, J.K. Nørskov, Using scaling relations to understand trends in the catalytic activity of transition metals, *J. Phys. Condens. Matter* 20 (2008) 64239, <http://dx.doi.org/10.1088/0953-8984/20/6/064239>.
- [60] M. Amft, S. Lebègue, O. Eriksson, N.V. Skorodumova, Adsorption of Cu, Ag, and Au atoms on graphene including van der Waals interactions, *J. Phys. Condens. Matter* 23 (2011) 395001, <http://dx.doi.org/10.1088/0953-8984/23/39/395001>.
- [61] M. Andersen, A.J. Medford, J.K. Nørskov, K. Reuter, Analyzing the case for bifunctional catalysis, *Angew. Chem. Int. Ed.* 55 (2016) 5210–5214, <http://dx.doi.org/10.1002/anie.201601049>.
- [62] M. Amft, B. Sanyal, O. Eriksson, N.V. Skorodumova, Small gold clusters on graphene: their mobility and clustering: a DFT study, *J. Phys. Condens. Matter* 23 (2011) 205301, <http://dx.doi.org/10.1088/0953-8984/23/20/205301>.
- [63] X. Tao, J. Wang, C. Liu, H. Wang, H. Yao, G. Zheng, Z.W. Seh, Q. Cai, W. Li, G. Zhou, C. Zu, Y. Cui, Balancing surface adsorption and diffusion of lithium-polysulfides on nonconductive oxides for lithium–sulfur battery design, *Nat. Commun.* 7 (2016) 11203, <http://dx.doi.org/10.1038/ncomms11203>.
- [64] J.K. Nørskov, F. Studt, F. Abild-Pedersen, T. Bligaard, Kinetics, *Fundam. Concepts Heterog. Catal.* John Wiley & Sons, Inc., 2014, pp. 68–84, <http://dx.doi.org/10.1002/9781118892114.ch5>.